

Article

Structural and Magnetic Properties of NiZn Ferrite Nanoparticles Synthesized by a Thermal Decomposition Method

JinAh Hwang ^{1,2} , Moonhee Choi ¹, Hyo-Soon Shin ¹, Byeong-Kwon Ju ^{2,*} and MyoungPyo Chun ^{1,*}

¹ Electronic Convergence Materials Division, Korea Institute of Ceramic Engineering and Technology, Jinju-si, Gyeongsangnam-do 660-031, Korea; fwangjin@korea.ac.kr (J.H.); moonhee77.choi@kicet.re.kr (M.C.); hshin@kicet.re.kr (H.-S.S.)

² Display and Nanosystem Laboratory, School of Electrical Engineering, Korea University, Seoul 13701, Korea

* Correspondence: bkju@korea.ac.kr (B.-K.J.); myoungpyo@kicet.re.kr (M.C.); Tel.: +82-2-3290-3237 (B.-K.J.); +82-55-792-2680 (M.C.)

Received: 7 August 2020; Accepted: 3 September 2020; Published: 9 September 2020



Abstract: Ni_{1-x}Zn_xFe₂O₄ (x = 0.5, 0.6, 0.7) nanoparticles were synthesized by a thermal decomposition method. The synthesized particles were identified as pure spinel ferrite structures by X-ray diffraction analysis, and they were calculated to be 46–51 nm in diameter by the Scherrer equation, depending on the composition. In the FE-SEM image, the ferrite nanoparticles have spherical shapes with slight agglomeration, and the particle size is about 50 nm, which was consistent with the value obtained by the Scherrer equation. The lattice parameter of the ferrite nanoparticles monotonically increased from 8.34 to 8.358 Å as the Zn concentration increased from 0.5 to 0.7. Initially, the saturation magnetization value slowly decreases from 81.44 to 83.97 emu/g, then quickly decreases to 71.84 emu/g as the zinc content increases from x = 0.5, through 0.6, to 0.7. Ni_{1-x}Zn_xFe₂O₄ toroidal samples were prepared by sintering ferrite nanoparticles at 1250 °C and exhibited faceted grain morphologies in the FE-SEM images with their grain sizes being around 5 μm regardless of the Zinc content. The real magnetic permeability (μ') of the toroidal samples measured at 5 MHz was monotonically increased from 106, through 150, to 217 with increasing the Zinc content from x = 0.5, through 0.6, to 0.7. The cutoff frequency of the ferrite toroidal samples was estimated to be about 20 MHz from the broad maximum point in the plot of imaginary magnetic permeability (μ'') vs. frequencies, which seemed to be associated with domain wall resonance.

Keywords: superparamagnetic; spinel ferrite; NiZn ferrite; nanoparticles

1. Introduction

Spinel ferrite nanoparticles such as NiZn, MnZn have gained much attention for several applications [1–5], including high frequency circuits, the cores of radiofrequency (RF) transformers, inductors, antennas and radar absorbing materials, based on their high resistivity and low loss at high frequency. They also have great potential as an efficient catalysts and/or catalyst supports for decomposing organic or inorganic pollutants [6,7]. NiZn ferrite nanoparticles are becoming more and more important in the field of bio-medical applications for instance magnetic resonance imaging (MRI), drug delivery systems and hyperthermia treatment of cancer by using their appropriate magnetic properties, antimicrobial activity and biological compatibility [8,9].

Figure 1 shows the spinel structure (the lattice parameter is about 0.84 nm) is formed by 24 cations (Fe²⁺, Zn²⁺, Co²⁺, Mn²⁺, Ni²⁺, Mg²⁺, Fe³⁺, Gd³⁺) and 32 O²⁻ anions and generally has a chemical form of AB₂O₄, which is designated as a cubic closed-packing of O²⁻ ions [10–13]. The round and

the square brackets represent the tetrahedral interstitial A site and the larger octahedral interstitial B site, respectively. Zinc ferrite is called a normal spinel structure of the form $ZnFe_2O_4$, where Zn^{2+} ions occupy the tetrahedral sites and Fe^{3+} ions occupy the octahedral sites [13]. Nickel ferrite is called an inverse spinel structure of the form $FeNiFeO_4$, where Ni^{2+} ions occupy the octahedral sites, and half the Fe^{3+} ions occupy the tetrahedral sites and the other half occupy the octahedral sites [10]. NiZn ferrite is a kind of solid solution composed of Ni ferrite and Zn ferrite, which can be expressed as the form $Zn_xFe_{(1-x)}Ni_{(1-x)}Fe_{(1+x)}O_4$. The magnetic properties of the NiZn ferrite are strongly dependent on the number of 3d unpaired electrons of transition metals. The Zn^{2+} ions do not have any unpaired electrons (or Bohr magneton) in the 3d orbital, while Ni^{2+} ions have two unpaired electrons and Fe^{3+} ions have five unpaired electrons in the 3d orbital. Therefore, the appropriate loading of the Ni^{2+} ion, which has unpaired electrons into the crystal structure of $ZnFe_2O_4$ provides much better magnetic properties, e.g., higher saturation magnetization (M_s) and lower coercivity (H_c) [14,15] because an addition of transition metal ions leads to the movement of some Fe^{3+} ions from the octahedral sites to the tetrahedral sites, and the unequal of Fe^{3+} ions in both lattice sites effectively produce the remainder of unpaired electrons, which generate and increase the magnetism [16].

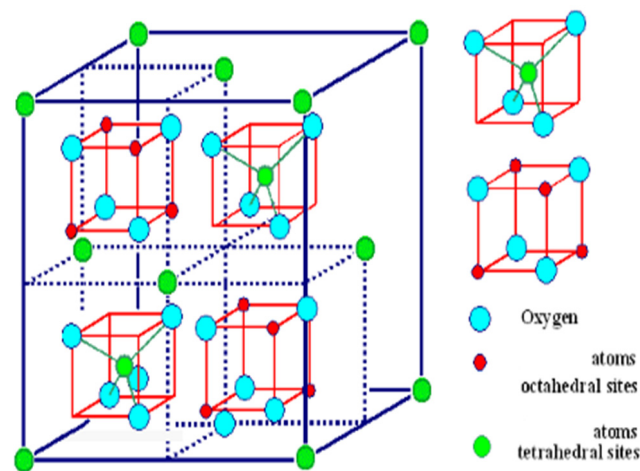


Figure 1. The spinel structure of ferrites is shown indicating the tetrahedral and octahedral sites.

In general, with a reduction in particle size, the coercive force gradually increases until it reaches the maximum value, but if the size of the particle is reduced to a critical size, the thermal effect becomes even more intense and produces super paramagnetic characteristics in which each particle becomes a single domain with not only very low magnetic loss but also very high magnetic permeability [17,18]. Moreover, the superparamagnetic particles have a zero coercive force and high magnetization, so the control of the particle size is very important because the properties of the nanocrystals strongly depend upon that. Properties of NiZn ferrite nanoparticles are greatly sensitive to the synthesis method and its preparation conditions. There are many methods for the synthesis of ferrite nanoparticles, including sol-gel, co-precipitation, high energy ball milling and thermal decomposition [19–23]. Thermal decomposition method has more advantages than other methods in synthesizing uniform and fine-nanoparticles with a high crystallinity. Also, it is easy to control particle size and particle size distribution with this method [24,25].

The morphology and composition of magnetic nanoparticles have a great influence on their magnetic properties not only in their own particles but also in bulk samples after sintering. When the saturation magnetization of magnetic nanoparticles increases, the initial permeability generally also increases according to the relationship of $\mu_i' = M_s D / K_1$, where $K_1 = M_s H_c / 0.96$ is the crystalline anisotropy constant, M_s is the saturation magnetization, H_c is the coercivity and D is the average grain size [26,27]. However, there are few studies available in the literature showing the relationship that the permeabilities of sintered magnetic samples are inversely proportional to their magnetization

value, and explaining the relationship in detail. Therefore, it seems to be beneficial studying NiZn ferrite systems showing these magnetic behavioral relationships in understanding and improving magnetic properties.

In this paper, we synthesized $\text{Ni}_{1-x}\text{Zn}_x\text{Fe}_2\text{O}_4$ ($x = 0.5, 0.6, 0.7$) ferrite nanoparticles by the thermal decomposition method and examined the influence of the Ni/Zn ratio on the crystal structures, microstructures and magnetic properties of the prepared NiZn ferrites using an X-ray diffractometer (XRD), a field emission scanning electron microscope (FE-SEM), an impedance analyzer and a vibrating sample magnetometer (VSM).

2. Materials and Methods

$\text{Ni}_{1-x}\text{Zn}_x\text{Fe}_2\text{O}_4$ ($x = 0.5, 0.6, 0.7$) nano-particles were synthesized by a thermal decomposition method as shown in Figure 2. The raw materials were nickel(II) acetylacetonate (97%), zinc acetylacetonate hydrate (95%), iron(III) acetylacetonate (97%). Oleic acid (90%) and oleylamine (70%) were used as a surfactant, 1,2-hexadecandiol (90%) as a reducing agent, and benzyl ether (98%) as a solvent. Ni, Zn and Fe-acetylacetonate precursors were weighed, respectively according to the chemical form of $\text{Ni}_{1-x}\text{Zn}_x\text{Fe}_2\text{O}_4$ ($x = 0.5, 0.6, 0.7$) and poured into a 500 mL three neck flask that was filled with a mixed solution of 6 mmol oleic acid, 6 mmol oleylamine, 1,2-hexadecandiol(HDD), and 20 mL benzyl ether. The precursor solution was heated to 200 °C for 1 h, then further heated to 300 °C and kept there for 1 h; the process was carried out in a N_2 atmosphere with refluxing using cooling water. The solution that finished the reaction was cooled to room temperature, centrifuged for 30 min at a speed of 4000 rpm and washed repeatedly with hexane and ethanol in order to separate organic remains from the ferrite particles. Hexane was used to dissolve fat acids such as oleic acid and oleylamine. Finally, $\text{Ni}_{1-x}\text{Zn}_x\text{Fe}_2\text{O}_4$ ($x = 0.5, 0.6, 0.7$) nanoparticles were collected and dried at 100 °C for 24 h.

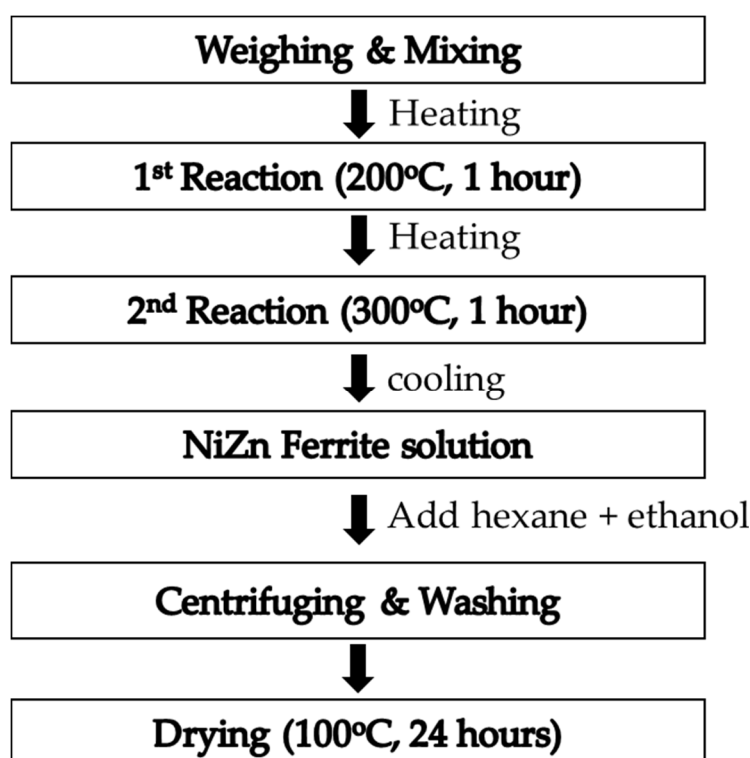


Figure 2. Experimental procedure for synthesizing $\text{Ni}_{1-x}\text{Zn}_x\text{Fe}_2\text{O}_4$ ($x = 0.3, 0.4, 0.5$) ferrite nanoparticles.

Toroidal samples of NiZn ferrites were fabricated by uniaxial pressing. The ferrite powder was mixed with a PVA (Polyvinyl alcohol, 5 wt %) binder solution, which was poured into a toroidal

shaped mold and applied with a pressure of 1 ton/cm² to make green toroidal samples. The green toroidal samples were burned out at 650 °C for 30 min in air and then sintered at 1250 °C for 2 h.

The phase purity of the NiZn ferrites nanoparticles was investigated with an X-ray diffractometer (XRD: D/max 2200 V/PC, Rigaku Co., Akishima, Japan). Microstructures of sintered toroidal ferrite samples were observed with a Scanning Electron Microscope (SEM, JSM 6700F, JEOL, Japan). Magnetic permeability (μ' , μ'') was measured from 1 MHz to 1 GHz with an Impedance analyzer (E4991A). Saturation magnetization of the ferrite particles was measured with a Vibrating Sample Magnetometer (VSM).

3. Results

Figure 3a–c shows the X-ray diffraction patterns of Ni_{1-x}Zn_xFe₂O₄ (x = 0.5, 0.6, 0.7) nanoparticles, which indicate a pure spinel structure for all three ferrites without any second phases regardless of the composition.

Figure 4 shows the dependence of the lattice parameters of the ferrite nanoparticles on the Ni concentration, which were calculated with the following equation [28].

$$a = \frac{\lambda \sqrt{h^2 + k^2 + l^2}}{2 \sin \theta_{hkl}}$$

The lattice parameter increases monotonically from 8.340 Å to 8.358 Å with increasing Zn concentration from x = 0.5 to 0.7, which is due to the fact that the ionic radius of the Zn²⁺ ion (0.74 Å) is larger than that of the Ni²⁺ ion (0.69 Å). This result means that some Zn ions appear to be incorporated into Ni site, considering that the larger Zn²⁺ ions prefer tetrahedral A-sites, but the smaller Ni²⁺ ions prefer octahedral B-sites in the crystalline spinel structure. The lattice volume of Ni_{1-x}Zn_xFe₂O₄ was also increased with increasing Zn concentration, which is reasonable considering the difference in their ionic radii.

Figure 5 shows the dependence of the crystallite size of ferrite nanoparticles on the Zn concentration, in which the average size (D) of crystallites was calculated from (311) peak using Scherer's equation as shown below.

$$D = \frac{k\lambda}{\beta \cos \theta}$$

where the constant $k = 0.89$, $\lambda = 1.5406$ Å, and β is the FWHM of the (311) diffraction peak. Regardless of the Zn concentration, the crystallite size was in the range of 46 to 51 nm and there was no significant difference in it.

Figure 6 shows the hysteresis curve of NiZn ferrite nanoparticles at room temperature. As the Zn ion concentration increases from x = 0.5 to 0.7 in Ni_{1-x}Zn_xFe₂O₄, the saturation magnetization and the coercivity decreases from 83 to 71 emu/g and from 18.54 to 16.48 O_e, respectively, which is considered high compared to some other results. The magnetic properties of the Ni_{1-x}Zn_xFe₂O₄ depends on its chemical composition, grain size, preparation method, and the arrangement of cation between two interstitial sites [29]. The ferrite under an applied field has two magnetization processes: domain wall motion and magnetization rotation within domains. In general, domain wall motion is sensitive to extrinsic material features such as grain size and grain-boundary structure, the presence of inclusions or pores within the grains, impurity levels and stresses. Figure 7 shows the Ni_{1-x}Zn_xFe₂O₄ particles are considered single domain particles, taking into account the fact that the crystallite size gotten from the XRD is almost the same as the particle size obtained from the FE-SEM image. Therefore, it appears that the high saturation magnetization is mainly due to an arrangement of cations on the sub-lattices A and B. The decrease in the saturation magnetization with Zn ion content is well complied with the report that the Curie temperature, which means the transition temperature between paramagnetic and ferromagnetic phase, decreases rapidly with increasing nonmagnetic Zn ions in NiZn ferrite [29].

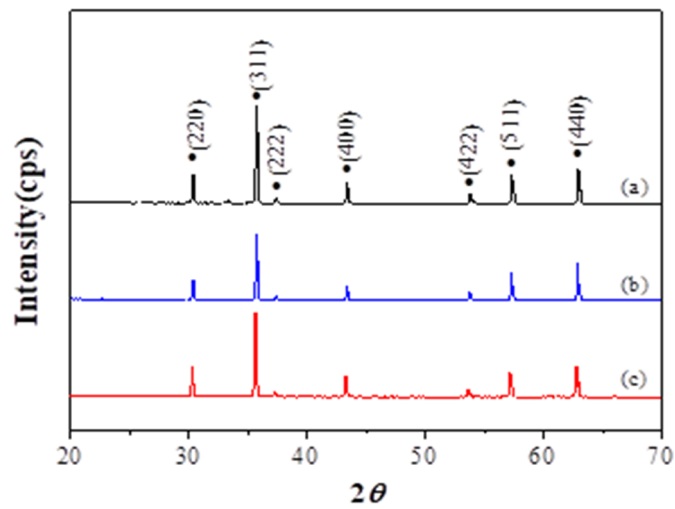


Figure 3. (a–c) X-ray diffraction patterns of $Ni_{1-x}Zn_xFe_2O_4$ ($x = 0.3, 0.4, 0.5$) nanoparticles of the synthesized samples: (a) $x = 0.3$, (b) $x = 0.4$, and (c) $x = 0.5$.

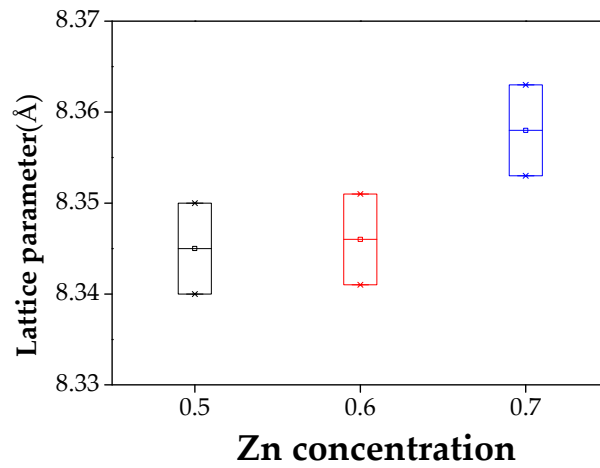


Figure 4. The dependence of the lattice parameters of the $Ni_{1-x}Zn_xFe_2O_4$ ($x = 0.5, 0.6, 0.7$) ferrite nanoparticles on the Zn concentration.

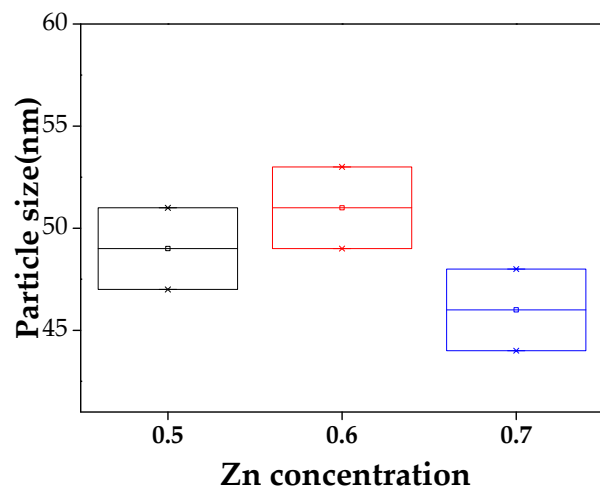


Figure 5. The dependence of the crystallite size of $Ni_{1-x}Zn_xFe_2O_4$ ($x = 0.5, 0.6, 0.7$) ferrite nanoparticles on the Zn concentration.

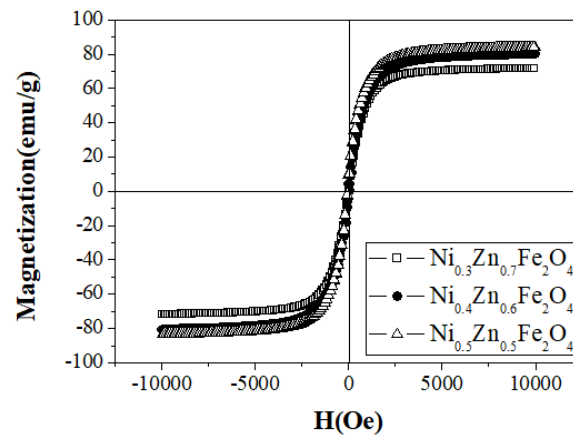


Figure 6. Hysteresis curves of $Ni_{1-x}Zn_xFe_2O_4$ ($x = 0.5, 0.6, 0.7$) ferrite nanoparticles.

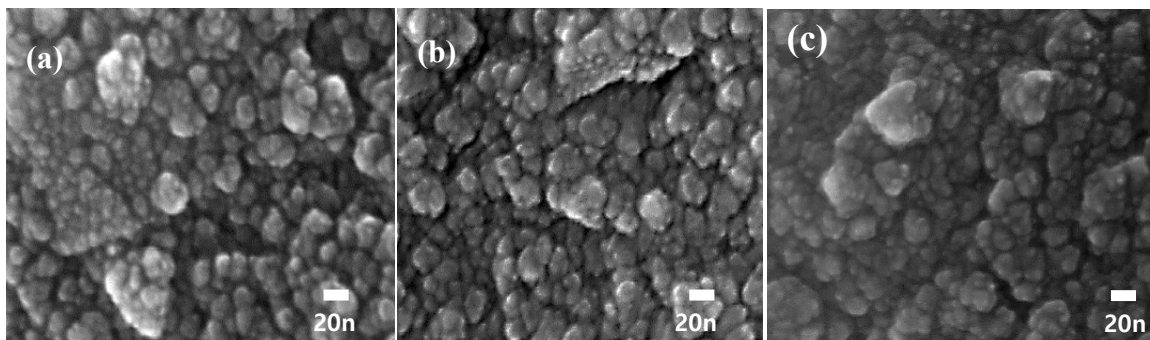
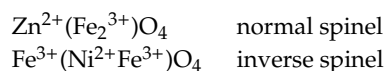


Figure 7. FE-SEM image of synthesized $Ni_{1-x}Zn_xFe_2O_4$ ($x = 0.5, 0.6, 0.7$) nanoparticles. (a) $x = 0.5$ (b) $x = 0.6$, and (c) $x = 0.7$.

The saturated magnetization of ferrite is proportional to the difference in sub-lattice magnetization associated with octahedral and tetrahedral sites. In normal spinel, tetrahedral sites are occupied by divalent cations, while in reverse spinel these sites are filled by trivalent cations. $ZnFe_2O_4$ is reported as normal spinel, but $NiFe_2O_4$ is inverse spinel. The combination of $ZnFe_2O_4$ and $NiFe_2O_4$ form a solid solution $Ni_{1-x}Zn_xFe_2O_4$. With increase in Zn content, Fe^{+3} in the tetrahedral sites are replaced by Zn^{2+} cations and Fe^{+3} fill the octahedral sites emptied by Ni^{2+} . Zn^{2+} ion doesn't contain any unpaired electrons, however, Ni^{2+} ion has two and Fe^{+3} ion has five unpaired electrons. The following convention has been adopted to define the location of cations in the octahedral and tetrahedral sites of ferrite:



where the ions on the octahedral sites are enclosed in brackets. Ferric ions may occupy tetrahedral or octahedral sites depending on the different cations present. When non-magnetic Zn ions are incorporated into the $NiFe_2O_4$ lattice, they have a stronger affinity for the tetrahedral site than ferric ions and thus will reduce the amount of Fe^{3+} ions on the tetragonal A-site. The net magnetic moment due to the number of unpaired electrons in nickel zinc ferrite is proportional to Equation (2). The Zn^{2+} ions have no unpaired electrons, while the Ni^{2+} ions have two unpaired electrons and the Fe^{3+} ions have five unpaired electrons [30]. Saturation magnetization is considered to increase with increasing Zn content according to Equations (1) and (2):

$$Zn_y^{2+} Fe_{1-y}^{3+} (Ni_{1-y}^{2+} Fe_{1+y}^{3+})O_4 \tag{1}$$

$$M = -0(y) - 5(1 - y) + 2(1 - y) + 5(1 + y) = 2 + 8 y \tag{2}$$

where y is the mole fraction of Zn^{2+} ions. The theoretical value of this magnetization was inconsistent with the magnetization data which indicates a decreasing trend with increasing Zn content. However, it has been reported that the magnetization of NiZn ferrite decreases as the Zn content increases above 0.5 mole fraction in NiZn ferrite [31]. At high levels of zinc substitution, Fe^{3+} ions in the tetragonal sites were so diluted that super-exchange interaction between tetrahedral and octahedral sites was lost and the saturation magnetization dropped. The Curie temperature declines abruptly and eventually drops below room temperature with increasing Zn content, so that the magnetic properties disappear at this temperature.

Figure 8a–c shows the X-ray diffraction patterns of the $Ni_{1-x}Zn_xFe_2O_4$ ($x = 0.5, 0.6, 0.7$) samples sintered at 1250 °C. There are no second phases in these X-ray diffraction patterns, which means that the sintered samples have the same pure spinel structure regardless of their composition.

Figure 9a–c displays FE-SEM images of the $Ni_{1-x}Zn_xFe_2O_4$ ($x = 0.5, 0.6, 0.7$) sintered at 1250 °C. Note that the microstructures become denser with an increasing Zn concentration in $Ni_{1-x}Zn_xFe_2O_4$ ferrite. This behavior is consistent with the study that Zn ions not only lower the sintering temperature, but also play a crucial role in increasing the sintering density. Meanwhile, it is interesting to note that although the particle size is somewhat uniform with about 5 μm , the particle shape is faceted.

Figure 10a,b shows the real and imaginary parts of the magnetic permeability of $Ni_{1-x}Zn_xFe_2O_4$ ($x = 0.5, 0.6, 0.7$) toroidal samples in the frequency range from 1 MHz to 1 GHz. It is clear from the Figure 10 that the real permeability (μ') at 5 MHz increases monotonically from $\mu' = 106$ to 217 with increasing Zn content from $x = 0.5$ to 0.7 in of $Ni_{1-x}Zn_xFe_2O_4$ ($x = 0.5, 0.6, 0.7$). The value of μ' for all three toroid samples remains constant up to 10 MHz and increases slightly with further increase in frequency.

The imaginary part of permeability (μ'') increases with increase in frequency and a broad maximum is observed at 20 MHz, where μ' decreases rapidly. This characteristic is a consequence of domain wall resonance, which consists of relaxation and resonance type dispersions. Hence, in the low frequency domain, the complex permeability spectrum of domain wall motion can be treated as the superposition of resonance and relaxation dispersion [30]. The broad maximum in μ'' is the result of the overlapping of the domain wall motion (DWM) resonance and spin resonance [32–35]. The contributions of domain wall motion on the complex permeability spectrum decreases gradually with increasing frequency, and only the spin rotational component becomes dominant at higher frequency [36]. At frequencies below 500 kHz, the chief magnetizing mechanism of ferrite is DMW [37], while the domain wall resonance happens in the range from 1 to 100 MHz and rotational resonance occurs above 1 GHz [32,33].

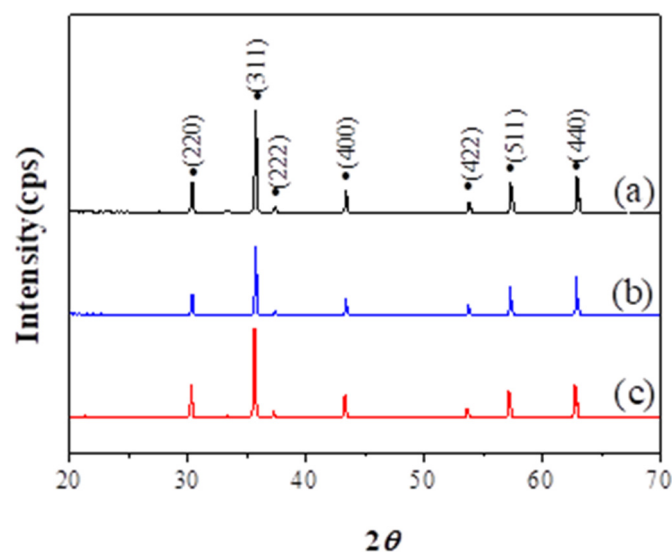


Figure 8. The X-ray diffraction patterns of the $Ni_{1-x}Zn_xFe_2O_4$ ($x = 0.5, 0.6, 0.7$) samples sintered at 1250 °C: (a) $x = 0.5$, (b) $x = 0.6$, and (c) $x = 0.7$.

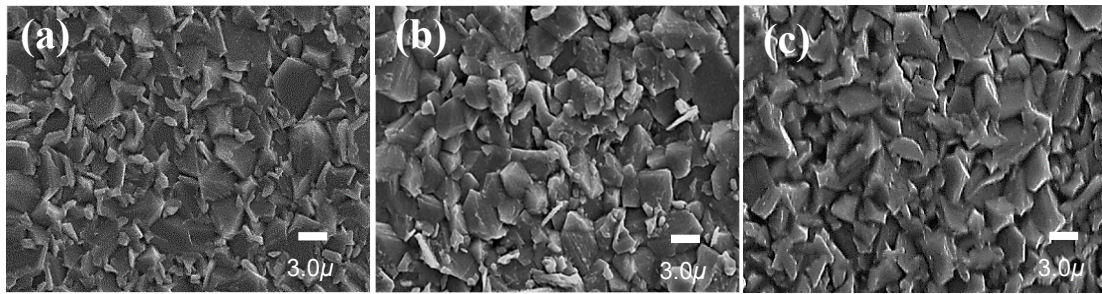


Figure 9. FE-SEM images of the $Ni_{1-x}Zn_xFe_2O_4$ ($x = 0.5, 0.6, 0.7$) samples sintered at $1250\text{ }^\circ\text{C}$: (a) $x = 0.5$, (b) $x = 0.6$, and (c) $x = 0.7$.

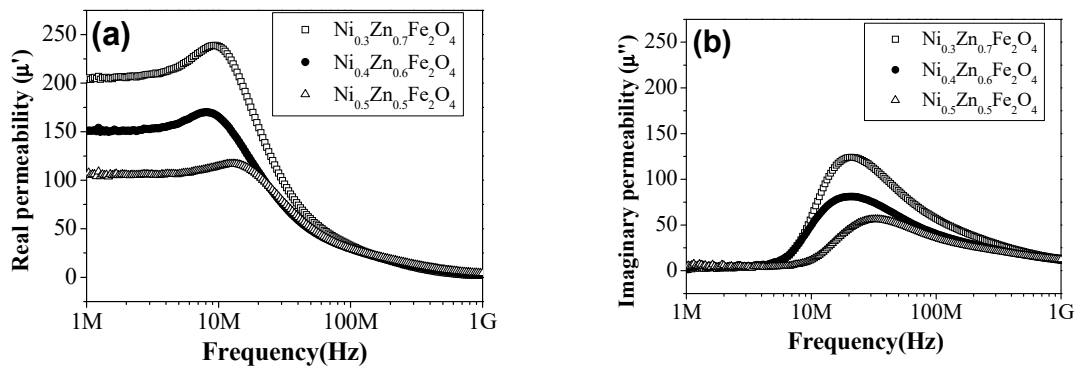


Figure 10. Real part (a), and imaginary part (b) of the magnetic permeability of $Ni_{1-x}Zn_xFe_2O_4$ ($x = 0.5, 0.6, 0.7$) toroidal samples in the frequency range from 1 MHz to 1 GHz.

The frequency dependence of the permeability of ferrite samples is connected to two types of magnetization mechanisms: domain wall motion and spin rotation, as shown below.

$$\mu = 1 + \chi_{dw} + \chi_{sp} \tag{3}$$

$$\chi_{dw} = \frac{3\pi M_s^2 D}{4\gamma} \tag{4}$$

$$\chi_{sp} = \frac{2\pi M_s^2}{K_u} \tag{5}$$

where χ_{dw} is the domain wall susceptibility, χ_{sp} is the intrinsic rotational susceptibility, K_u is the anisotropy constant, γ is the gyromagnetic ratio, M_s is the saturation magnetization, and D is the grain diameter. With increasing Zn content, μ' of $Ni_{1-x}Zn_xFe_2O_4$ ($x = 0.5, 0.6, 0.7$) increases, while the cut-off frequency decreases. Real part of permeability (μ') is depends on various parameters such as stoichiometry, grain size, composition, porosity, impurity levels, saturation magnetization, magnetostriction, and crystal anisotropy [37]. Higher permeabilities are favored by large grain size, low porosity, high saturation magnetization, low crystalline anisotropy, low magnetostriction and high purity. In particular, the real part of permeability strongly depends on grain size.

As Zn ion increases, the crystalline anisotropy is decreased, but permeability is increased as shown in Table 1. Here, the crystalline anisotropy constant K_1 was calculated using the following relation [38] expressed as $K_1 = M_s H_c / 0.96$, where M_s is the saturation magnetization and H_c is the coercivity. The initial permeability varies inversely with magneto-crystalline anisotropy constant, but proportional to grain size according to the relationship [39] represented by $\mu_i' = M_s D / K_1$ where D is the average grain size. Thus, the formula $\mu_i' = 0.96 D / H_c$ is obtained, which means that as the Zn concentration increases, the increase in permeability (μ') is related to increased grain size and reduced coercivity. This corresponds to the results shown in Table 1. In other words, an increase in μ' as the Zn

concentration increases can be attributed to an increase in the domain wall mobility promoted by the larger grains, as well as lower crystalline anisotropy according to Equations (1) and (2).

Table 1. Properties of $\text{Ni}_{1-x}\text{Zn}_x\text{Fe}_2\text{O}_4$ ($x = 0.5, 0.6, 0.7$) powder and toroidal samples.

Sample Name	Saturation Magnetization M_s (emu/g)	Lattice Parameter a (Å)	Crystallite Size (nm)	Permeability μ' (5MHz)	Coercivity H_c (Oe)	Anisotropic Constant K_1 (erg/cm ³)
$\text{Ni}_{0.5}\text{Zn}_{0.5}\text{Fe}_2\text{O}_4$	84.44	8.340	49	106	18.54	1631
$\text{Ni}_{0.4}\text{Zn}_{0.6}\text{Fe}_2\text{O}_4$	83.97	8.346	51	150	17.56	1536
$\text{Ni}_{0.3}\text{Zn}_{0.7}\text{Fe}_2\text{O}_4$	71.84	8.358	46	217	16.48	1233

4. Conclusions

$\text{Ni}_{1-x}\text{Zn}_x\text{Fe}_2\text{O}_4$ ($x = 0.5, 0.6, 0.7$) nanoparticles were successfully synthesized by a thermal decomposition method and they were identified as pure spinel ferrite structures by X-ray diffraction analysis. The synthesized ferrite nanoparticles were calculated to be 46–51 nm in diameter by the Scherrer equation, which was consistent with the particle size of about 50 nm observed from FE-SEM images. The lattice parameters of ferrite nanoparticles monotonically increased as the Zn content increased. The synthesized ferrite nanoparticles showed relatively high saturation magnetization values of 71–83 emu/g depending on their composition. Toroidal samples were prepared by sintering ferrite nanoparticles at 125 °C, and they exhibited faceted grain morphology in FE-SEM images with a grain size of about 5 μm . The real magnetic permeability (μ') of the toroidal sample measured at 5 MHz increased with increasing Zn content, showing $\mu' = 217$ for $x = 0.7$. The cutoff frequency of the ferrite toroidal sample was about 20 MHz, which seemed to be associated with domain wall resonance.

Author Contributions: Conceptualization, M.C. (Moonhee Choi); methodology, J.H.; validation, J.H.; formal analysis, H.-S.S.; investigation, H.-S.S.; writing—original draft preparation M.C. (MyoungPyo Chun); writing—review and editing, B.-K.J. and M.C. (MyoungPyo Chun). All authors have read and agreed to the published version of the manuscript.

Funding: This work was supported by the Technology Innovation (20010938, Development of 630 V high capacity MLCC array module for power train), funded by the Ministry of Trade, Industry & Energy (MOTIE, Sejong City, Korea).

Conflicts of Interest: The authors declare no conflict of interest.

References

- Gubbala, S.; Nathani, H.; Koziol, K.; Misra, R.D.K. Magnetic properties of nanocrystalline Ni–Zn, Zn–Mn, and Ni–Mn ferrites synthesized by reverse micelle technique. *Phys. B Condens. Mater.* **2004**, *348*, 317. [[CrossRef](#)]
- Costa, A.C.F.M.; Morelli, M.R.; Kiminami, R.H.G.A. Microstructure and magnetic properties of $\text{Ni}_{(1-x)}\text{Zn}_x\text{Fe}_2\text{O}_4$ synthesized by combustion reaction. *J. Mater. Sci.* **2007**, *42*, 779. [[CrossRef](#)]
- Goldman, M.; DeVitre, R.; Tenca, J. Materials Science Cement Distribution and Bond Strength in Cemented Posts. *J. Dent. Res.* **1984**, *63*, 582.
- Han, D.H.; Luo, H.I.; Yang, Z. Remanent and anisotropic switching field distribution of platelike Ba-ferrite and acicular particulate recording media. *J. Magn. Magn. Mater.* **1996**, *161*, 376. [[CrossRef](#)]
- Yaun, T.; Wei, Z.; Yuan, J.; Yan, L.; Liu, Q.; Wang, J. The microstructure and magnetic properties of $\text{Ni}_{0.4}\text{Zn}_{0.6}\text{Fe}_2\text{O}_4$ films prepared by spin-coating method. *J. Sol-Gel Sci. Technol.* **2011**, *58*, 501. [[CrossRef](#)]
- Shangguan, W.F.; Teraoka, Y.; Kagaw, S. Promotion effect of potassium on the catalytic property of CuFe_2O_4 for the simultaneous removal of NO_x and diesel soot particulate. *Appl. Catal. B Environ.* **1998**, *16*, 149. [[CrossRef](#)]
- Cui, H.-J.; Shi, J.-W.; Yuan, B.; Fu, M.-L. Synthesis of porous magnetic ferrite nanowires containing Mn and their application in water treatment. *J. Mater. Chem. A* **2013**, *1*, 5902. [[CrossRef](#)]

8. Nowicka, A.; Kowalczyk, A.; Donten, M.; Krysinski, P.; Stojek, Z. Influence of a Magnetic Nanoparticle as a Drug Carrier on the Activity of Anticancer Drugs: Interactions of Double Stranded DNA and Doxorubicin Modified with a Carrier. *Anal. Chem.* **2009**, *81*, 7474–7483. [[CrossRef](#)]
9. Sunkara, B.; Misra, R. Enhanced antibactericidal function of W^{4+} -doped titania-coated nickel ferrite composite nanoparticles: A biomaterial system. *Acta Biomater.* **2008**, *4*, 273–283. [[CrossRef](#)] [[PubMed](#)]
10. Carta, D.; Loche, D.; Mountjoy, G.; Navarra, G.; Corrias, A. NiFe₂O₄ Nanoparticles Dispersed in an Aerogel Silica Matrix: An X-ray Absorption Study. *J. Phys. Chem. C* **2008**, *112*, 15623–15630. [[CrossRef](#)]
11. Kaur, B.; Arora, M.; Shankar, A.; Srivastava, A.K.; Pan, R.P. Induced Size Effects of Gd³⁺ ions Doping on Structural and Magnetic Properties of Ni-Zn Ferrite Nanoparticles. *Adv. Mater. Lett.* **2012**, *3*, 399–405. [[CrossRef](#)]
12. Goswami, P.P.; Choudhury, H.A.; Chakma, S.; Moholkar, V.S. Sonochemical Synthesis and Characterization of Manganese Ferrite Nanoparticles. *Ind. Eng. Chem. Res.* **2013**, *52*, 17848–17855. [[CrossRef](#)]
13. Silva, F.G.D.; Depeyrot, J.; Campos, A.F.C.; Aquino, R.; Fiorani, D.D. PeddisStructural and magnetic properties of spinel ferrite nanoparticles. *J. Nanosci. Nanotechnol.* **2019**, *19*, 4888–4902. [[CrossRef](#)] [[PubMed](#)]
14. Akhtar, M.J.; Nadeem, M.; Javaid, S.; Atif, M. Cation distribution in nanocrystalline ZnFe₂O₄ investigated using X-ray absorption fine structure spectroscopy. *J. Phys. Condens. Matter* **2009**, *21*, 405303. [[CrossRef](#)] [[PubMed](#)]
15. Cullity, B.D.; Graham, C.D. *Introduction to Magnetic Materials*, 2nd ed.; John Wiley & Sons Inc.: New York, NY, USA, 2009.
16. Nakashima, S.; Fujita, K.; Tanaka, K.; Hirao, K.; Yamamoto, T.; Tanaka, I. First-principles XANES simulations of spinel zinc ferrite with a disordered cation distribution. *Phys. Rev. B* **2007**, *75*. [[CrossRef](#)]
17. Hasirci, C.; Karaagac, O.; Köçkar, H. Superparamagnetic zinc ferrite: A correlation between high magnetizations and nanoparticle sizes as a function of reaction time via hydrothermal process. *J. Magn. Magn. Mater.* **2019**, *474*, 282–286. [[CrossRef](#)]
18. Rameshbabu, R.; Ramesh, R.; Kanagesan, S.; Karthigeyan, A.; Ponnusamy, S. Synthesis of superparamagnetic ZnFe₂O₄ nanoparticle by surfactant assisted hydrothermal method. *J. Mater. Sci. Mater. Electron.* **2013**, *24*, 4279–4283. [[CrossRef](#)]
19. Rostamnejadi, A.; Salamati, H.; Kameli, P.; Ahmadvand, H. Superparamagnetic behavior of La_{0.67}Sr_{0.33}MnO₃ nanoparticles prepared via sol-gel method. *J. Magn. Magn. Mater.* **2009**, *321*, 3126–3131. [[CrossRef](#)]
20. Zheng, Z.; Zhong, X.; Zhang, Y.; Yu, H.; Zeng, D. Synthesis, structure and magnetic properties of nanocrystalline Zn_xMn_{1-x}Fe₂O₄ prepared by ball milling. *J. Alloy. Compd.* **2008**, *466*, 377–382. [[CrossRef](#)]
21. Gao, R.-R.; Zhang, Y.; Yu, W.; Xiong, R.; Shi, J. Superparamagnetism and spin-glass like state for the MnFe₂O₄ nano-particles synthesized by the thermal decomposition method. *J. Magn. Magn. Mater.* **2012**, *324*, 2534–2538. [[CrossRef](#)]
22. Kozlov, D.A.; Shcherbakov, A.B.; Kozlova, T.O.; Angelov, B.; Kopitsa, G.P.; Garshev, A.V.; Baranchikov, A.E.; Ivanova, O.S.; Ivanov, V.K. Photochromic and Photocatalytic Properties of Ultra-Small PVP-Stabilized WO₃ Nanoparticles. *Molecules* **2019**, *25*, 154. [[CrossRef](#)]
23. Padmapriya, G.; Manikandan, A.; Krishnasamy, V.; Jaganathan, S.K.; Antony, S.A. Spinel Ni_xZn_{1-x}Fe₂O₄ (0.0 ≤ x ≤ 1.0) nano-photocatalysts: Synthesis, characterization and photocatalytic degradation of methylene blue dye. *J. Mol. Struct.* **2016**, *1119*, 39–47. [[CrossRef](#)]
24. Slatineanu, T.; Iordan, A.; Palamaru, M.N.; Caltun, O.F.; Gafton, V.; Leontie, L. Synthesis and characterization of nanocrystalline Zn ferrites substituted with Ni. *Mater. Res. Bull.* **2011**, *46*, 1455–1460. [[CrossRef](#)]
25. Gubanova, N.; Baranchikov, A.E.; Kopitsa, G.P.; Almasy, L.; Angelov, B.; Ivanov, V.K.; Rosta, L.; Ivanov, V.K. Combined SANS and SAXS study of the action of ultrasound on the structure of amorphous zirconia gels. *Ultrason. Sonochem.* **2015**, *24*, 230–237. [[CrossRef](#)]
26. Singh, A.K.; Goel, T.C.; Mendiratta, R.G. Low-temperature synthesis of Mn_{0.2}Ni_{0.2}Zn_{0.6}Fe₂O₄ ferrites by citrate precursor method and study of their properties. *Phys. Status Solidi (a)* **2004**, *201*, 1453–1457. [[CrossRef](#)]
27. Pujar, R.B.; Kulkarni, S.N.; Bellad, C.B.; Chougule, B.K. Compositional, temperature and frequency dependence of initial permeability in Zr⁴⁺ substituted Mg-Zn ferrites. *J. Mater. Sci. Lett.* **1997**, *16*, 1668–1699. [[CrossRef](#)]
28. Velmurugana, K.; Venkatachalapathy, V.S.K.; Sendhilnathanc, S. Thermogravimetric and Magnetic Properties of Ni_{1-x}Zn_xFe₂O₄ Nanoparticles Synthesized by Coprecipitation. *Mater. Res.* **2009**, *12*, 529–534. [[CrossRef](#)]

29. Verma, A.; Goel, T.; Mendiratta, R.; Alam, M. Dielectric properties of NiZn ferrites prepared by the citrate precursor method. *Mater. Sci. Eng. B* **1999**, *60*, 156–162. [[CrossRef](#)]
30. Stoner, E.C. *Introduction to Magnetic Materials*; Addison-Wesley: Boston, MA, USA, 1972; pp. 183–187.
31. Guillaud, C. Propriétés Magnétiques des Ferrites. *J. Phys. Radium* **1951**, *12*, 239–248. [[CrossRef](#)]
32. Tsutaoka, T. Frequency dispersion of complex permeability in Mn–Zn and Ni–Zn spinel ferrites and their composite materials. *J. Appl. Phys.* **2003**, *93*, 2789–2796. [[CrossRef](#)]
33. Su, H.; Zhang, H.; Tang, X.; Jing, Y. Influence of microstructure on permeability dispersion and power loss of NiZn ferrite. *Appl. Phys.* **2008**, *103*, 093903. [[CrossRef](#)]
34. Nakamura, T. Snoek's limit in high-frequency permeability of polycrystalline Ni–Zn, Mg–Zn, and Ni–Zn–Cu spinel ferrites. *J. Appl. Phys.* **2000**, *88*, 348. [[CrossRef](#)]
35. Lebourgeois, R.; Coillot, C. Mn–Zn ferrites for magnetic sensor in space applications. *J. Appl. Phys.* **2008**, *103*, 07E510. [[CrossRef](#)]
36. Verma, A.; Chatterjee, R. Effect of zinc concentration on the structural, electrical and magnetic properties of mixed Mn–Zn and Ni–Zn ferrites synthesized by the citrate precursor technique. *J. Magn. Magn. Mater.* **2006**, *306*, 313–320. [[CrossRef](#)]
37. Shaikh, P.A.; Kambale, R.C.; Rao, A.V.; Kolekar, Y.D. Effect of Ni doping on structural and magnetic properties of $\text{Co}_{1-x}\text{Ni}_x\text{Fe}_{1.9}\text{Mn}_{0.1}\text{O}_4$. *J. Magn. Magn. Mater.* **2010**, *322*, 718. [[CrossRef](#)]
38. Byun, T.Y.; Bycon, S.C.; Hong, K.S. Factors affecting initial permeability of Co-substituted Ni–Zn–Cu ferrites. *IEEE Trans. Magn.* **1999**, *35*, 3445. [[CrossRef](#)]
39. Guyot, M.; Globus, A. Wall displacement and bulging in magnetization mechanisms of the hysteresis loop. *Phys. Status Solidi B* **1972**, *52*, 427.



© 2020 by the authors. Licensee MDPI, Basel, Switzerland. This article is an open access article distributed under the terms and conditions of the Creative Commons Attribution (CC BY) license (<http://creativecommons.org/licenses/by/4.0/>).